PAPER

Check for updates

Hygromechanical deformation of wood cell walls regulated by the microfibril angle†

RongZhuang Song,‡ ZeZhou He,‡ JiaHao Li, YuanZhen Hou, HengAn Wu [ID] and YinBo Zhu*

Wood, a ubiquitous biomaterial, exhibits exceptional mechanical and functional properties owing to its hierarchical microstructure. Understanding the mechanisms underlying wood moisture absorption is crucial for advancing the application of wood-based materials, yet the process has been hindered by the intricate interplay between microstructure, moisture dynamics, and deformation. Here, we employed large-scale molecular dynamics simulations to comprehensively investigate the hygromechanical deformation of wood cell walls, accounting for the coupled effects of microfibril angle (MFA) and hygroscopicity difference in the main microstructural components: hemicellulose and cellulose nanofibril. Our molecular model, incorporating the practical microstructure and mass fractions of the two main components, provides quantitative insights previously unaddressed. We identified three key mechanisms by which MFA influences wood cell wall deformation. This influence occurs through the regulation of water molecule diffusion stemming from the competition of hydrogen bonds among cellulose nanofibrils, hemicellulose, and their interfaces. At low moisture levels, void filling promotes intermolecular cross-linking, leading to slight structural contraction. At high moisture levels, the impact of MFA becomes pronounced, affecting water absorption behavior, saturation moisture content, and the degree of deformation. Furthermore, the swelling deformation of wood cell walls can be further enhanced by improving hemicellulose content and optimizing MFA to below 23°. Our study underscores the crucial role of MFA in the moisture absorption of wood and establishes a theoretical foundation for the design and optimization of biomimetic materials and humidity-controlled robots.

1. Introduction

Wood has extensive applications in construction, engineering, and energy due to its unique microstructure, hygromechanics, thermal properties, and biodegradability.[1–6] As depicted in Fig. 1, the wood cell walls feature a hierarchical structure across various scales,[7–9] comprising multiple layers with stiff cellulose nanofibrils (CNFs) embedded in a polymer matrix primarily made of hemicellulose and lignin.[10,11] The distinctive structural arrangement endows wood with numerous mechanical and functional advantages, such as a high strength-to-weight ratio, remarkable toughness, and excellent thermal and acoustic insulation properties.[12,13] Additionally, wood exhibits anisotropic mechanical behavior and unique hygroscopic characteristics, offering vast potential for designing and modifying wood-based materials, such as thermal insulation, ion transport, and optical materials.[14–20] These desirable properties and the

stability of wood cell walls are largely influenced by their microstructure and moisture content.[4,21] Therefore, a comprehensive understanding of the interplay between microstructure and hygromechanics is crucial for designing wood-based materials with tailored characteristics suitable for various applications like moisture-responsive actuators, agricultural sowing, and smart building materials.[22–25]

The microstructure of the wood cell walls, particularly the S2 layer, plays a pivotal role in determining the overall structural performance.[10] As the thickest layer, the S2 layer is primarily composed of CNFs with varying microfibril angles (MFAs) and hemicellulose. The MFA (θ), illustrated in Fig. 1, refers to the angle between the aligned fibers and the axial direction, typically ranging from 0° to 45° depending on wood species and growth conditions.[26] Both MFA and moisture content significantly influence the stability and behavior of wood cell walls.[27] For instance, wood with a higher MFA tends to exhibit greater longitudinal shrinkage during drying and lower tensile strength, while wood with a lower MFA is generally stiffer and more dimensionally stable.[28–30] Besides, Meng et al. systematically investigated how MFAs influence the fracture toughness of cellulose nanopaper, revealing key insights into the MFA-property relationships in wood-based materials.[5] Water

CAS Key Laboratory of Mechanical Behavior and Design of Materials, Department of Modern Mechanics, University of Science and Technology of China, Hefei 230027, China. E-mail: zhuyinbo@ustc.edu.cn

† Electronic supplementary information (ESI) available. See DOI: https://doi.org/10.1039/d4ta07560a

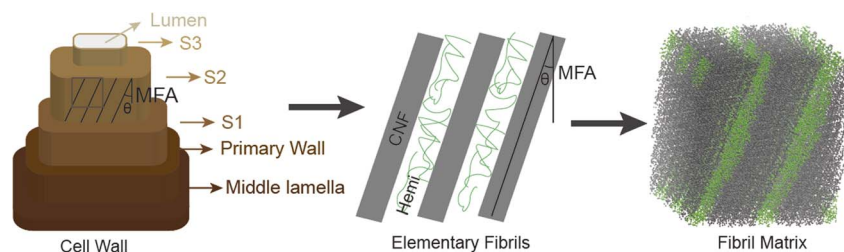‡ These authors contributed equally to this work.

Fig. 1 Schematic diagram of the hierarchical structure of wood cell walls. The molecular model of the S2 layer microstructure contains the CNFs and hemicellulose molecular chains, and the MFA (θ) and moisture content are two main factors when considering the deformation behavior of the S2 layer microstructure in wood cell walls.

molecules interact intricately with the microstructural components, significantly affecting its swelling behavior and overall stability.[31–33] The coupling between MFA and moisture content not only impacts the mechanical properties but also governs water diffusion and hydrogen bond formation at the nanoscale.[34] Understanding these factors is essential for predicting wood behavior under varying environmental conditions.

Several theoretical models have been developed to describe directional movement and stress generation in plant cells, particularly focusing on the role of microfibril angle in the dimensional stability of wood.[28,35] Early models highlighted the anisotropic shrinkage of wood and its relationship with MFA, revealing intricate connections among wood microstructure, hygroscopic behavior, and dimensional changes.[36,37] Simplified models incorporating extensible cellulose fibrils within an isotropically swelling matrix accounted for MFA distribution and reproduced experimental observations, such as swelling degrees and humidity-induced bending movements.[38] However, these models often overlook detailed internal structural components and the complex interactions between water and cell wall constituents, which impact the anisotropic mechanical properties and the reliability of predictions. Recent advancements include autonomous devices that leverage the coupling between humidity and MFA for efficient seed sowing.[23] Despite these developments, quantitatively elucidating the hygromechanical mechanisms of wood cell walls at the molecular level remains challenging due to theoretical and experimental limitations.[39]

Atomic-scale simulations are crucial for establishing quantitative relationships between theoretical predictions and experimental observations, providing deep insights into the molecular organization of materials. Recent studies have employed molecular dynamics (MD) simulations and poromechanics to reveal the coupling of sorption and deformation in soft nanoporous polymers, emphasizing the significant role of hydrogen bonds (HBs).[40] Zhang *et al.* systematically investigated the hygromechanical mechanisms of wood cell walls, developing numerical frameworks to analyze multicomponent natural biocomposites.[41] Their study significantly clarified how moisture-induced swelling and mechanical deformation interact, revealing the roles of cellulose, hemicellulose, and lignin in material behavior.[41] However, a comprehensive investigation integrating the effects of MFA, moisture diffusion, and hydrogen bonding is still lacking. Multidisciplinary approaches are needed to thoroughly understand the interplay between microstructure and moisture conditions, which will clarify the significant roles of wood cell wall components and MFAs in moisture response and guide enhancements in wood-based material performance.

In what follows, we conducted large-scale MD simulations to investigate the deformation of wood cell walls under the influence of internal MFA and external moisture. Our model consists of alternating cellulose fibrils and hemicelluloses in a mass ratio of 4 : 1, with an MFA ranging from 0° to 45°.[4] Given the inherent hydrophobicity of lignin,[41] the potential impacts of lignin–water interactions remain an open area of investigation and will be addressed in future research. Simulated wide-angle X-ray diffraction (XRD) was calculated using the Debyer software package.[42] The nanoscale deformation characteristics of the cell wall's internal structure, changes in HBs between CNFs, hemicellulose, and water, and the overall system's scale changes during swelling were quantitatively analyzed. Key patterns observed from extensive simulations included the impact of MFA on the swelling scale and deformation direction, varying degrees of deformation under different moisture levels, and the movement of water molecules guided by HBs competition. These findings elucidate the mechanism by which the interaction of MFA and water regulates the deformation of wood cell walls. The obtained insights here aim to offer novel design concepts for developing biomimetic materials derived from wood, and establish a theoretical foundation to advance the chemical modification of biomass and material synthesis.

2.   Models and methods

2.1.   Model preparation

A two-phase MD model consisting of crystalline CNF and non-crystalline hemicellulose (galactoglucomannan) was proposed to analyze the moisture-induced wood cell walls behavior.[43] The detailed modeling steps are described in Section S1 of the ESI.† While the precise structure of the wood cell walls remains a matter of debate due to limitations in contemporary experimental techniques for accurately measuring nanoscale interactions,[41] fibril bundles composed of crystalline cellulose and hemicellulose provide a strong and reliable framework for studying moisture-related phenomena in wood.[43,44] In MD simulations, the continuous mobility of molecules makes maintaining a stable volume fraction challenging. Hence, the

mass fraction of CNF and hemicellulose is regulated to ensure consistency in the simulations. The simulation boxes were solvated using TIP3P water molecules.[45]

The selection of galactoglucomannan (GGM) was based on its prevalence as one of the most abundant types of hemicellulose found in plant cell walls.[46] A single GGM chain comprising 11 monomers was constructed using CHARMM-GUI.[47] This GGM chain features a random polymerization of glucose and mannose monomers in a 1 : 4 ratio, with branched galactose side groups attached to the mannose units, constituting approximately 8 wt% of the structure.[43] Each fibril was constructed using the cellulose-builder program, comprising 20 cellulose chains arranged in the cellulose Iβ crystal lattice.[48] These chains were organized in a 1-2-3-4-4-3-2-1 parallel configuration within each hydrogen-bonded layer. Initial cellulose fibrils and randomly distributed hemicellulose were assembled by Packmol.[49] The assembly method is shown in Fig. 1. The solid matrix density ranges from 1.41 g cm^{-3} to 1.42 g cm^{-3}, which is consistent with the experimentally measured data within a small error range.[50]

2.2. MD simulations

MD simulations were performed using LAMMPS software.[51] Interactions among atoms were modeled using the CHARMM force field, renowned for its efficacy in large-scale nanocellulose simulations.[52–54] Periodic boundary conditions were applied in all directions, with covalent bonds at the boundaries in the y and z directions forming periodic cross-links to simulate infinite model conditions (Fig. S1–S5†). The time step of MD simulations was set as 1 fs. Water molecules were introduced to both sides of the initial anhydrous system at mass fractions of 5%, 10%, 15%, 20%, and 25% (Fig. S6†). Moisture content (MC) is defined as the ratio of the mass of water to the total mass of carbohydrates. Further swelling deformations were analyzed at five additional MC levels: 20%, 22.5%, 25%, 27.5%, and 30%. As the water content increased beyond 25%, no significant changes were observed in the number of hydrogen bonds between water molecules and CNF or hemicellulose, nor in the overall strain. This indicated that the system had reached saturation. The system first underwent energy minimization to ensure the minimum energy state and internal stress. Then the equilibration lasted for 100 ns was performed in an isothermal–isobaric (NPT) ensemble at 300 K temperature and a zero pressure, ensuring a complete reaction between water molecules and the S2 structure. All simulation results were visualized by the OVITO and VMD software.[55,56] The potential energy of CNF and the local strain distribution were calculated using the built-in programs of LAMMPS and OVITO,[51,55] respectively. The wetting time referred to the elapsed time after water was added. H-bonds were identified using VMD software based on the criteria for effective H-bonds, which were defined as having an oxygen–oxygen distance (d_{OO}) of less than 3.5 Å and an angle between the hydrogen bond donor, hydrogen, and acceptor atoms (θ_{OHO}) greater than 150°.[56,57] The torsion angles of O5–C5–C6–O6 and C4–C5–C6–O6 were obtained using the ISAACS software.[58]

3. Results and discussion

3.1. Hydration behavior and molecular deformation

In the first series of MD simulations, we focused on the deformation behavior of the S2 layer microstructure. The model, shown in Fig. 1, mainly contains alternating layers of nanocellulose and hemicellulose, with MFA and moisture content as two key factors. Since the range of MFA in wood cell walls typically ranges from 0° to 45°, we here selected several representative MFAs in our simulations. Fig. 2a shows the morphological changes of the microstructure under different moisture contents and MFAs, indicating that the deformation behavior varies significantly with different MFAs and moisture levels. The microstructure with an MFA of 45° exhibits minimal deformation. For MFAs below 45°, the swelling behavior can be divided into two stages: initially, water molecules enter the existing nanovoids between cellulose nanofibril (CNF) and hemicellulose, causing the hemicellulose to swell until the nanovoids are saturated; in the second stage, additional water enlarges these nanovoids, causing an obvious separation between adjacent CNFs. The morphology snapshots in Fig. 2a and the strain distributions in Fig. 2b show that when the MFA is between 0 and 45°, swelling in the y-direction is accompanied by shrinkage in the z-direction, and the shrinkage strain ($\gamma_{zz} = -0.035$) is much smaller than the swelling strain ($\gamma_{yy} = 0.116$). Additionally, the MFAs also slightly change with the swelling process. As shown in Fig. 2c, the MFA changes during the saturation stage vary depending on the initial MFA. When the initial MFA is 0°, it remains essentially unchanged. For initial MFAs between 7.5° and 30°, the maximum change ranges from 4° to 5°. Beyond 37.5°, the MFA change decreases, becoming nearly zero at an initial MFA of 45°. This variation aligns with the degree of swelling deformation (Fig. 2a), indicating that greater deformation correlates with more significant changes in MFA. The increase of MFA will lead to a reduction in axial load capacity, indicating that the evolution of MFA is a significant factor in how water affects the mechanical properties of wood cell walls.[41,59]

To further investigate the impact of wetting under different MFAs on the stability of the CNF structure at the atomic scale, we systematically analyzed the potential energy and CNF conformational changes. Based on the calculated torsion angles of O5–C5–C6–O6 and C4–C5–C6–O6 (Fig. S7†), Fig. 2e and f present the conformation percentage variations of two different hydroxymethyl groups with increasing moisture content.[60] When MFAs are below 30°, the TG conformation (where 'G' is *gauche* and 'T' is *trans*), which forms the structural basis for O5–H···O3 and O6–H···O2 HBs, decreases by 20–25%. The rotation of the O6 group causes the TG conformation to transition to GT and GG conformations, as depicted in Fig. S7.† Although the TG conformation has the lowest energy in an isolated molecule, it becomes less stable in polar solvents like water.[61] Fig. 2d shows the changes in the potential energy of CNF. For MFAs below 30°, CNF energy is significantly affected by wetting. As moisture content increases from 0% to 15%, the energy decreases rapidly. Beyond 15% moisture content, the energy decrease slows down
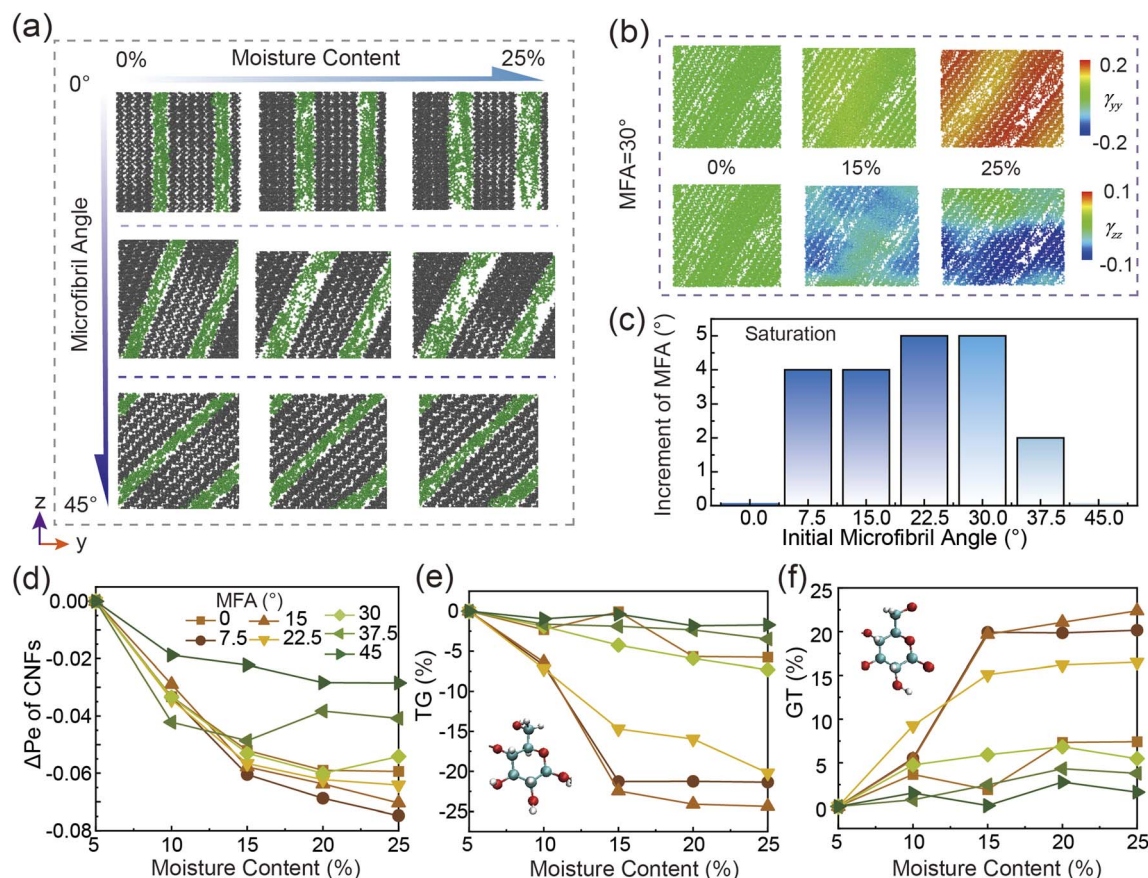
Fig. 2 Deformation behavior of the S2 layer microstructure. (a) Deformation modes under different moisture contents and MFAs. (b) Strain distributions (γ_{yy} and γ_{zz}) during the swelling process. Here MFA = 30° is selected as an example and the moisture contents are 0%, 15%, and 25%, respectively. (c) MFA increments of simulated molecular models reach the saturated state. (d) Potential energy increment (ΔPe) of CNFs as a function of moisture content. (e) The change of TG (here 'G' is *gauche* and 'T' is *trans*) conformations as a function of moisture content. (f) The change of GT conformations as a function of moisture content. The symbols in (d–f) denotes different MFAs in molecular models.

or stabilizes. The similar change trend between CNF energy and TG conformational transition suggests that TG's transition to other conformations in a humid environment involves a reaction with negative entropy.[61]

Hydrogen-bonding network among CNF and hemicellulose is crucial for the mechanical properties of wood cell walls. To understand the evolution of hydrogen-bonding network during swelling process, we counted different types of HBs under several moisture contents. Fig. 3a–c illustrates the various HBs between CNFs, hemicellulose, and water molecules. In the simulation model without water, CNF and hemicellulose form original HBs through their abundant –OH groups, classified as CNF–CNF, CNF–Hemi, and Hemi–Hemi HBs. The introduction of water molecules disrupts the original hydrogen-bonding network, leading to the formation of bridging HBs such as CNF–Water–CNF, CNF–Water–Hemi, and Hemi–Water–Hemi HBs. The density evolution of water molecules in the *yz* plane was analyzed to understand the movement of water within the microstructure models, using a system with an MFA of 22.5° as an example (Fig. 3d). Initially, water molecules are approximately uniformly distributed throughout the system. Over time, distinct contour lines emerge locally at the CNF–Hemi interface,

while the number of HBs between water molecules decreases rapidly (Fig. 3e). Concurrently, the number of CNF–CNF, CNF–Hemi, and Hemi–Hemi HBs also decreases sharply, whereas the number of CNF–Water and Hemi–Water HBs continues to increase (Fig. S8†). These observations indicate that HBs form more readily between carbohydrates and water molecules than between water molecules themselves. During the middle stage, water molecules move from the surface of the microstructure to the internal CNF–Hemi interface while maintaining stable CNF–Water and Water–Water HBs (Fig. 3e and S8†). The stronger competitive ability of hydrogen-bonding formation at the CNF–Hemi interface directs the gradual migration of water molecules towards this interface, thereby increasing the chances for hemicellulose to bond with water molecules. This process results in a clear boundary in the density distribution of water molecules (Fig. 3d) and a continuous increase in Hemi–Water HBs (Fig. S8†). The bonding of water molecules with hemicellulose fills internal voids within the hemicellulose, causing it to swell (Fig. S9†).

The saturation stage is marked by an increase in Water–Water HBs, indicating that the binding between water molecules and carbohydrates is nearing saturation. At this stage,
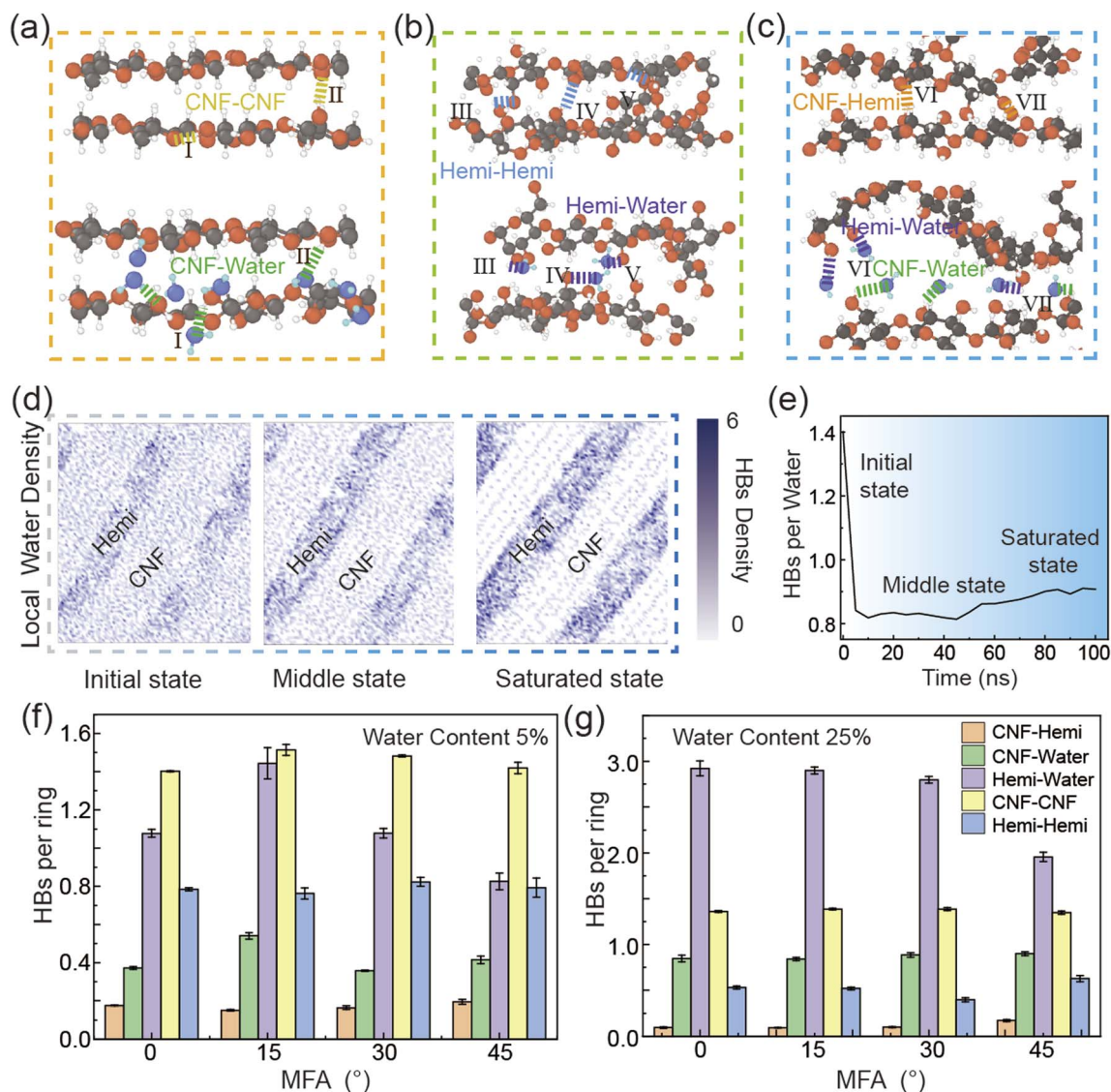
Fig. 3 Hydrogen-bonding behavior. (a–c) Schematic diagram of water molecules entering the CNF–Hemi interlayers and replacing the original HBs (CNF–CNF, Hemi–Hemi, and CNF–Hemi) to form bridging HBs among CNF, Water, and Hemi. The colored short dash lines highlight different types of HBs. (d) Local density distribution of water molecules under different states. The color bar represents the number of water molecules. (e) The number of HBs per water molecule as a function of water addition time. (f and g) The number of each type of HBs per ring as a function of MFA with the moisture content of 5% and 25%, respectively. Error bars correspond to standard deviation. MFA = 22.5° with MC = 25% is taken as an example.

water molecules continue to infiltrate the microstructure, with hydrogen bonding between hemicellulose and water molecules guiding their movement due to the saturation of interfacial HBs. As more water molecules fill the original voids between hemicellulose, larger voids are created. This exacerbates the swelling of hemicellulose and increases the spacing between CNFs (Fig. 3d and S9†). Fig. 3f, g and S10–S12† illustrate the variation in the number of each type of HBs per ring with MFA at different moisture levels. The most notable changes are observed in Hemi–Water HBs at different moisture levels. At the maximum moisture content of 25%, the number of Hemi–Water HBs peaks in microstructures with MFAs between 0° and 30° and decreases for MFAs greater than 30°, reaching its lowest

point at 45°. Conversely, CNF–Hemi HBs exhibit an inverse trend, peaking at 45° under maximum moisture content. These trends in HBs variation align precisely with the swelling behavior of hemicellulose shown in Fig. 2a. This alignment suggests that MFA affects the binding of water molecules to the internal components of the wood cell walls *via* HBs, thereby influencing water movement within the structure and consequent structural deformation.

3.2. Characterization of hydration deformation

To understand the molecular-level interactions between CNFs and water, XRD scattering intensities were computed in simulations to assess configuration changes in CNFs with varying

moisture levels. XRD profiles for four different MFAs were selected to compare these variations over wetting time (Fig. 4a–d). Four diffraction peaks were calibrated according to the monoclinic indexation.[62] The results indicate that the impact of water molecules on crystal configurations is significant, as all peaks vary with the increase in wetting time regardless of the MFA. The most affected peaks are $(1\bar{1}0)$ and (110). When the MFA is below 35°, the $(1\bar{1}0)$ peak weakens while the (110) peak intensifies over time, a pattern most pronounced at an MFA of ~22.5° (Fig. 4c). The fusion of the $(1\bar{1}0)$ peak into the (110) peak leads to notable increases in the intensity and width of the (110) peak. Changes in diffraction peak intensity suggest variations in lattice spacing corresponding to these diffraction planes. These variations likely result from the disordering of the molecular structure (Fig. 4i and S13†). By correlating the visualized molecular structure with the diffraction data, it can be inferred that the large rotation of cellulose groups induced by water molecules causes the absence and merging of diffraction peaks.

When the MFA exceeds 35° (Fig. 4d), both the $(1\bar{1}0)$ and (110) peaks intensify and sharpen. This can be attributed to the degree of binding between CNF and water molecules at different MFAs. As shown in Fig. 3f, g, S11, and S12† (green strips), when the moisture content increases from 5% to 25%, the number of HBs per ring between CNFs and water increases by only 0.88 times for an MFA of 37.5°, compared to 1.42 times increase for an MFA of 22.5°. Thus, the structural influence of water molecules on models with MFAs above 30° appears less significant. Unlike the changes observed in the $(1\bar{1}0)$ and (110)

peaks, the (200) and (004) peaks remain relatively stable. The (200) peak generally weakens slightly and shifts to a smaller angle, indicating a larger separation between parallel cellulose sheets. Values of the d-spacing of each peak were calculated using Bragg's law for quantitative analysis, representing the distance between planes reflecting incident X-rays.[63,64] Fig. 4e–h show the shifts in d-spacing over wetting time for the $(1\bar{1}0)$, (110), (200), and (004) peaks. Notably, the data fluctuations for an MFA of 37.5° are minimal compared to other MFAs, consistent with the XRD results (Fig. 4a–d). Peak fusion causes some $d_{1\bar{1}0}$ data to be missing in the later stages of wetting, but a decreasing trend for $d_{1\bar{1}0}$ is still evident. Although both d_{200} and d_{110} show significant growth towards the end compared to the initial wetting stage, this growth is not positively correlated with wetting time. The transient increase in d_{200} and d_{110} stabilizes or decreases after reaching a critical value.

Combining the theory proposed by Abe et al.[65] along with the mechanism of water molecule movement guided by HBs competition (Fig. 3d), it can be inferred that in the early stages of wetting, CNFs have abundant opportunities to interact with water molecules. Meanwhile, the swelling of hemicellulose is confined to the filling of pre-existing voids by water molecules, thereby limiting the degree of swelling. This process causes the expansion of the crystal, resulting in an increase in d-spacing. As water molecules continue to penetrate the gaps between CNFs and hemicellulose, enlarging the pre-existing voids, the intense swelling of the hemicellulose restricts the expansion of CNFs and subjects them to compression. Consequently, the d-
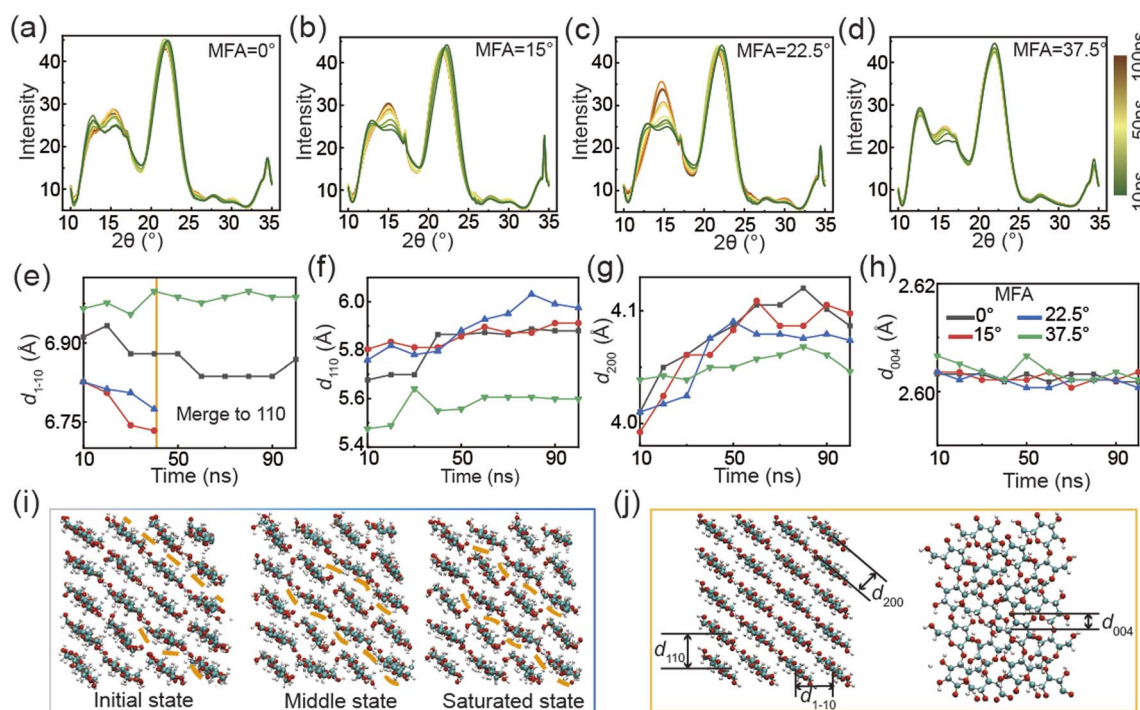

Fig. 4 Moisture-MFA-dependence of the crystalline parameters based on molecular models. Computed wide-angle X-ray diffraction (XRD) spectral curves under different MFAs and infiltration times. (e–h) Lattice parameters ($d_{1\bar{1}0}$, d_{110}, d_{200}, and d_{004}) determined from computed scattering intensities. Taking the model with an MFA of 22.5° as an example. (i) Changes in the morphology of CNFs under different state. In (e–i), MFA = 22.5° with MC = 25% is taken as an example. (j) Schematic diagram of typical directions in the crystal.

spacing will show a downward trend. This behavior is consistent with previous studies, where no significant change in the lattice spacing of the (004) peak upon wetting was detected.[63] As shown in Fig. 4j, the main interactive force of the (004) planes is generated by strong covalent bonds. Compared to other planes controlled by van der Waals or hydrogen bonding interactions, the (004) planes are more resistant to external distortion, such as wetting. Our MD simulations, combined with literature review,[33,41] reveal the hydration-induced deformation of wood cell walls. To facilitate applications such as seeding robots, we proposed a phase diagram that intuitively illustrates the contributions of humidity, MFA, and volume fraction to the deformation.

3.3. Hygromechanical constitutive relation of MFA

The deformation of the wood cell walls with moisture at different MFAs was summarized in Fig. 5. Fig. 5a can help us deconstruct the hygromechanical deformation of wood cell walls engineered by the inner microstructure MFA. This effect can be summarized in three aspects:

(i) Swelling and shrinking: when the MFA is below 45°, wood cell wall tends to swell with moisture. In contrast, when the MFA exceeds 45°, wood cell wall tends to shrink. The magnitude of swelling is four to five times greater than that of shrinkage.

(ii) Saturation water absorption capacity: the MFA significantly impacts the water absorption capacity of wood cell walls. Specifically, wood cell wall with an MFA of 45° exhibits the lowest water absorption and minimal deformation during infiltration. In contrast, when the MFA ranges from 0° to 22.5°, the wood cell walls display the highest absorbency, achieving a final saturated moisture content of approximately 25%. This finding aligns with experimentally observed maximum equilibrium moisture content values.[1]

(iii) Deformation degree: significant discrepancies exist in deformation among wood cell walls with different MFAs at identical moisture content levels. For example, wood cell walls exhibit similar deformation degrees when the MFA ranges from 0° to 15°. However, deformation peaks when the MFA is approximately 22.5°. Beyond 30°, the deformation trend diminishes until the strain nearly reaches zero at 45°.

The diagram of deformation strain *versus* MFA in Fig. 5a can elucidate how plants like pine cones and wheat awns naturally curve. The influence of the MFA on the swelling of the wood cell wall structure is reflected not only in the degree of hemicellulose swelling (Fig. 2a) but also in the configuration changes of CNFs (Fig. 2e–f and 4a–h). The inset structure diagram in Fig. 5a illustrates the deformation evolution of the microstructure with varying MFAs as moisture content increases. The relationship between uniaxial strain and moisture is notably non-linear. At moisture content levels below 10%, even with an MFA below 45°, the strain value remains nearly zero or may even be negative. Initially, water molecules entering the system primarily fill voids and cannot induce significant swelling (Fig. 2a). Rapid establishment of HBs between water molecules and carbohydrates tightens the connections between wood cell wall components, causing the system to shrink under low
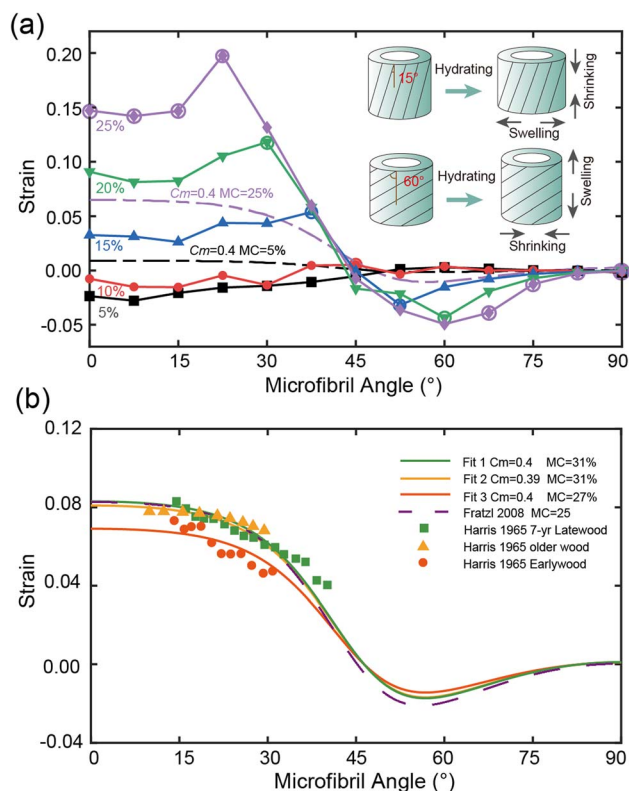

Fig. 5 Summary of the swelling and shrinking deformation of wood cell walls regulated by MFA and moisture content synergistically. (a) The hygromechanical deformation captured by molecular simulations. The solid lines with symbols show that uniaxial (transverse) strain of wood cell walls as functions of MFA considering different moisture contents. The circles denote that simulation models reach the saturation state. The dotted lines present the strain predictions at different MFAs, which are given by rule of mixtures analysis (RoM) different colors correspond to different moisture contents (MC). The inset gives the schemes of swelling and shrinking of hydrated wood cell walls. Due to the model's symmetry, the transverse strain values from MFAs of 45° to 90° are equivalent to the longitudinal strain values from MFAs of 0° to 45°. (b) Comparison of experimental data[29] with theoretical models. The different colored points represent experimental data from various wood types, while the solid lines show fits of this data using RoM, with volume fractions and moisture content labeled. Dashed lines represent the fitting curves derived from the Fratzl model.[38]

moisture conditions, referred to as the moisture-dominated deformation phase. As more water molecules penetrate the microstructure, they expand and multiply already saturated voids, resulting in significant swelling. This stage is referred to as the coupling stage of MFA and moisture.

Furthermore, we used the Rule of Mixtures (RoM) to analyze the swelling strain by considering the volume fractions of CNF and hemicellulose.[41,66] This analysis allows us to derive a quantitative relationship between the swelling strain and the MFA at different moisture levels. The detailed derivation process and the resulting formula are provided in Section S3 of the ESI.† The final theoretical prediction of the strain value can be expressed as:

$$\varepsilon_1 = f(c_\mathrm{m}, \varphi, \nu, \theta, \eta). \tag{1}$$

Here ν represents the Poisson coefficient of the hemicellulose matrix, φ represents the elastic modulus ratio of CNF and hemicellulose, c_m represents the volume fraction of hemicellulose, θ represents microfibril angle, η represents the isotropic volume strain due to swelling of the matrix, ε_1 represents swelling strain in the global direction.

We compared the MD simulation results with theoretical predictions based on the RoM, as shown in Fig. 5a. While the RoM aligns with MD simulations in predicting strain direction relative to the MFA, the strain values deviate significantly. This discrepancy arises primarily due to the volume fraction used in the RoM, set at $c_m = 0.4$ based on empirical data and the actual composition of plant cell walls.[67] Accurately quantifying this volume fraction during simulations is challenging. The inability to standardize the volume fraction contributes to this deviation. Additionally, the porosity of the actual microstructure and dynamic changes in HBs between CNF, hemicellulose, and water molecules impact the final deformation. These factors are challenging to incorporate into theoretical models, leading to the observed differences. Notably, the MD results indicate that when the MFA is about 22.5°, the swelling strain reaches an extreme value, which is not reflected in theoretical predictions. Table S2† summarizes the experimental hygromechanical behavior in relation to the MFA. Both Leonardon et al. and Luo et al. observed strain extremes occurring around 22°.[23,68] Similarly, the Fratzl model predicts that maximum tensile stress occurs at an MFA of approximately 25°, supporting the presence of an extreme swelling value within this range.[38]

Fig. 5b presents the experimental strain data caused by moisture changes,[29] alongside fitted lines from the RoM for each dataset. For comparison, theoretical values from the Fratzl model are also included.[38] Both the experimental data and theoretical models follow the same trend as the MD simulations: at a constant moisture level, varying the MFA alters strain behavior, while changes in moisture at a fixed MFA affect strain magnitude. The fitting results suggest that Fratzl's theory applies only to specific cases with certain volume fractions. A comparative analysis of the Fratzl model and swelling-strain curves derived from the RoM for volume fractions of 0.8 and 0.4 (Fig. S14†) shows that our model captures a wider range of deformation as the hemicellulose volume fraction increases.[38] This highlights the critical role of hemicellulose in cell wall swelling, where higher hemicellulose content enhances swelling, resulting in larger deformation under identical humidity conditions.

The moisture content obtained from experimental fitting reached 31% (Fig. 5b), exceeding the 25% maximum water absorption predicted by MD simulations (Fig. 5a). This discrepancy is reasonable for several reasons. First, molecular simulations operate on a microscopic scale, whereas experimental data and theoretical models reflect macroscopic behavior. Scale effects can naturally introduce deviations between these two levels of analysis. Additionally, experimental conditions—such as temperature, pressure, and humidity—are often less controlled than the idealized conditions used in molecular simulations, further contributing to the observed differences. Variability among experimental results is also common, and discrepancies between experimental and simulated values are to be expected.

Combining our simulation results with theoretical predictions can clarify the principles behind the automatic seeding carriers developed by Luo et al. and allows for further optimization based on specific needs.[23] These carriers' ability to repeatedly bend and recover in response to changes in moisture is fundamentally due to the differing MFAs of the inner and outer layers. When ambient moisture changes, the strain mismatch between these layers causes the carriers to bend and return to their original shape, enabling them to drill into the soil. Based on the coupling mechanism we proposed, higher hemicellulose content increases the structure's sensitivity to moisture in bionic designs inspired by wood cell walls. Structures with MFAs between 0–23° exhibit greater uniaxial deformation compared to those with MFAs around 45° at the same moisture level. Therefore, for the active layer that drives bending in the automatic seeding carrier, the MFA should be set between 0–23°. In contrast, to minimize excessive deformation in the passive layer, hemicellulose content can be reduced, and the MFA can be set at about 45° to decrease moisture sensitivity. This insight enables the design of biomimetic wood-based materials by strategically arranging the MFA distribution and hemicellulose ratio, allowing for precise control over material deformation and an automatic response to changes in environmental humidity.

4. Conclusion

In summary, we conducted MD simulations to investigate the coupling effect of MFAs and hydration on the swelling deformation of wood cell walls by considering crucial molecular composition factors within the internal microstructure. Although theory predicts continuous expansion in structures with MFAs below 45° during water absorption, our results reveal significant swelling differences across moisture levels, driven by internal voids in the microstructure. At low moisture levels, void filling promotes intermolecular cross-linking, resulting in slight structural contraction. Conversely, at high moisture levels, the expansion of saturated voids induces significant structural swelling. More interestingly, the competition mechanism of HBs among CNF, hemicellulose, and their interfaces guides the movement of water molecules, playing a crucial role in the swelling deformation of the wood cell walls. The distribution of water molecule density over time indicates that the CNF–Hemi interface exhibits stronger attraction to water molecules compared to hemicellulose alone, which promotes water molecule binding to hemicellulose.

The unique real-time monitoring advantages of MD simulations have enabled a broader range of deformation to be achieved compared to what is challenging to obtain in experiments. Integrating the XRD data of CNF with the characteristics of molecular simulation structures indicates that the interaction between CNF and water molecules primarily induces changes in molecular groups of CNFs, while the swelling deformation of CNF is influenced by the swelling deformation of hemicellulose. The MFA significantly regulates the swelling

behavior of wood cell walls *via* the movement of water molecules driven by HBs competition, which affects the swelling of hemicellulose and the interactions between water molecules and CNF groups. The influence of MFA can be summarized in three key points: (i) water absorption behavior: when the MFA is greater than 45°, the material contracts transversely; when it is less than 45°, the material swells transversely. (ii) Saturation moisture content: the level of saturation moisture content varies depending on the MFA. (iii) Degree of deformation: different MFAs result in varying degrees of deformation at the same moisture content, with the maximum strain occurring near an MFA of 22.5°. Overall, our study highlights the crucial regulatory role of internal structural MFA of wood cell walls on their deformation behavior in humid environments. Our findings provide valuable insights into the hygromechanical behavior of wood cell walls at the nanoscale, enabling quantitative predictions that promise to facilitate the design and application of wood-based materials.

Data availability

The data supporting this article have been included as part of the ESI.†

Author contributions

RongZhuang Song: methodology, software, investigation, data curation, writing – original draft. ZeZhou He: methodology, funding acquisition, data curation, writing – review & editing. JiaHao Li: methodology. YuanZhen Hou: methodology. HengAn Wu: conceptualization, resources, project administration, funding acquisition, writing – review & editing. YinBo Zhu: conceptualization, methodology, validation, formal analysis, visualization, supervision, funding acquisition, writing – review & editing.

Conflicts of interest

The authors declare that they have no known competing financial interests or personal relationships that could have appeared to influence the work reported in this paper.

Acknowledgements

References

1 E. T. Engelund, L. G. Thygesen, S. Svensson and C. A. S. Hill, *Wood Sci. Technol.*, 2012, **47**, 141–161.

2 S. Ling, D. L. Kaplan and M. J. Buehler, *Nat. Rev. Mater.*, 2018, **3**, 1–15.

3 H. L. Zhu, W. Luo, P. N. Ciesielski, Z. Q. Fang, J. Y. Zhu, G. Henriksson, M. E. Himmel and L. B. Hu, *Chem. Rev.*, 2016, **116**, 9305–9374.

4 U.S. Department of Agriculture, Forest Service, *Wood Handbook: Wood as an Engineering Material*, 1987.

5 Q. H. Meng, B. Li, T. Li and X. Q. Feng, *Eng. Fract. Mech.*, 2018, **194**, 350–361.

6 Q. Meng and X. Shi, *J. Mech. Phys. Solids*, 2023, **173**, 105205.

7 J. Garemark, J. E. Perea-Buceta, M. Felhofer, B. Chen, M. F. Cortes Ruiz, I. Sapouna, N. Gierlinger, I. A. Kilpelainen, L. A. Berglund and Y. Li, *ACS Nano*, 2023, **17**, 4775–4789.

8 F. Barthelat, Z. Yin and M. J. Buehler, *Nat. Rev. Mater.*, 2016, **1**, 1–16.

9 F. J. Martin-Martinez, K. Jin, D. L. Barreiro and M. J. Buehler, *ACS Nano*, 2018, **12**, 7425–7433.

10 S. J. Booker and R. E, *Holz Roh- Werkst.*, 1998, **56**, 1–8.

11 J. Fahlén and L. Salmén, *J. Plant Biol.*, 2008, **4**, 339–345.

12 Q. H. Meng and T. J. Wang, *Appl. Mech. Rev.*, 2019, **71**, 040801.

13 D. Dai and M. Fan, in *Natural Fibre Composites*, 2014, pp. 3–65, DOI: 10.1533/9780857099228.1.3.

14 T. Li, Y. Zhai, S. M. He, W. T. Gan, Z. Y. Wei, M. Heidarinejad, D. Dalgo, R. Y. Mi, X. P. Zhao, J. W. Song, J. Q. Dai, C. J. Chen, A. Aili, A. Vellore, A. Martini, R. G. Yang, J. Srebric, X. B. Yin and L. B. Hu, *Science*, 2019, **364**, 760–763.

15 M. Zhu, J. Song, T. Li, A. Gong, Y. Wang, J. Dai, Y. Yao, W. Luo, D. Henderson and L. Hu, *Adv. Mater.*, 2016, **28**, 5181–5187.

16 T. Li, X. Zhang, S. D. Lacey, R. Mi, X. Zhao, F. Jiang, J. Song, Z. Liu, G. Chen, J. Dai, Y. Yao, S. Das, R. Yang, R. M. Briber and L. Hu, *Nat. Mater.*, 2019, **18**, 608–613.

17 S. Kim, K. Kim, G. Jun and W. Hwang, *ACS Nano*, 2020, **14**, 17233–17240.

18 J. Li, Y. Hou, Z. He, H. Wu and Y. Zhu, *Nano Lett.*, 2024, **24**, 6262–6268.

19 H. Liu, C. Chen, H. Wen, R. Guo, N. A. Williams, B. Wang, F. Chen and L. Hu, *J. Mater. Chem. A*, 2018, **6**, 18839–18846.

20 Y. Li, X. Yang, Q. Fu, R. Rojas, M. Yan and L. Berglund, *J. Mater. Chem. A*, 2018, **6**, 1094–1101.

21 Y. Hou, Q. F. Guan, J. Xia, Z. C. Ling, Z. He, Z. M. Han, H. B. Yang, P. Gu, Y. Zhu, S. H. Yu and H. Wu, *ACS Nano*, 2021, **15**, 1310–1320.

22 C. Chen, Y. Kuang, S. Zhu, I. Burgert, T. Keplinger, A. Gong, T. Li, L. Berglund, S. J. Eichhorn and L. Hu, *Nat. Rev. Mater.*, 2020, **5**, 642–666.

23 D. Luo, A. Maheshwari, A. Danielescu, J. Li, Y. Yang, Y. Tao, L. Y. Sun, D. K. Patel, G. Y. Wang, S. H. Yang, T. Zhang and L. Yao, *Nature*, 2023, **614**, 463–470.

24 A. Holstov, B. Bridgens and G. Farmer, *Constr. Build. Mater.*, 2015, **98**, 570–582.

25 D. Correa, A. Papadopoulou, C. Guberan, N. Jhaveri, S. Reichert, A. Menges and S. Tibbits, *3D Print Addit. Manuf*, 2015, **2**, 106–116.

26 P. Fratzl and R. Weinkamer, *Prog. Mater. Sci.*, 2007, **52**, 1263–1334.

27 W DJC, The physics of shape changes in biology PhD thesis, University of Potsdam, 2016.

28 N. F. Barber and B. A. Meylan, *Holzforschung*, 1964, **18**, 145–156.

29 J. M. Harris and B. A. Meylan, *Holzforschung*, 1965, **19**, 144–153.

30 D. I. Cowdrey, *Wood Sci. Technol.*, 1968, **2**, 268–278.

31 P. A. Penttila, A. Paajanen and J. A. Ketoja, *Carbohydr. Polym.*, 2021, **251**, 117064.

32 K. Kulasinski, D. Derome and J. Carmeliet, *J. Mech. Phys. Solids*, 2017, **103**, 221–235.

33 A. Paajanen, A. Zitting, L. Rautkari, J. A. Ketoja and P. A. Penttila, *Nano Lett.*, 2022, **22**, 5143–5150.

34 H. Wang, Z. Yu, X. Zhang, D. Ren and Y. Yu, *Holzforschung*, 2017, **71**, 491–497.

35 B. A. Meylan, *Wood Sci. Technol.*, 1972, **6**, 293–301.

36 H. Yamamoto, F. Sassus, M. Ninomiya and J. Gril, *Wood Sci. Technol.*, 2001, **35**, 167–181.

37 H. Yamamoto, *Wood Sci. Technol.*, 1999, **33**, 311–325.

38 P. Fratzl, R. Elbaum and I. Burgert, *Faraday Discuss.*, 2008, **139**, 275–282.

39 M. Sedighi-Gilani and P. Navi, *Wood Sci. Technol.*, 2006, **41**, 69–85.

40 M. Chen, B. Coasne, D. Derome and J. Carmeliet, *J. Mech. Phys. Solids*, 2020, **137**, 103830.

41 C. Zhang, M. Chen, S. Keten, B. Coasne, D. Derome and J. Carmeliet, *Sci. Adv.*, 2021, **7**, eabi8919.

42 M. Wojdyr, Debyer, 2020, **https://debyer.readthedocs.io/en/latest/**.

43 C. Zhang, M. Chen, B. Coasne, S. Keten, D. Derome and J. Carmeliet, *Composites, Part B*, 2022, **228**, 109449.

44 C. Zhang, M. Chen, S. Keten, D. Derome and J. Carmeliet, *NPG Asia Mater.*, 2021, **13**, 74.

45 P. Mark and L. Nilsson, *J. Phys. Chem. A*, 2001, **105**, 9954–9960.

46 A. Khodayari, W. Thielemans, U. Hirn, A. W. Van Vuure and D. Seveno, *Carbohydr. Polym.*, 2021, **270**, 118364.

47 S. Jo, T. Kim, V. G. Iyer and W. Im, *J. Comput. Chem.*, 2008, **29**, 1859–1865.

48 T. C. Gomes and M. S. Skaf, *J. Comput. Chem.*, 2012, **33**, 1338–1346.

49 L. Martínez, R. Andrade, E. G. Birgin and J. M. Martínez, *J. Comput. Chem.*, 2009, **30**, 2157–2164.

50 W. Zillig, Moisture transport in wood using a multiscale approach PhD thesis, Catholic University of Leuven, 2009.

51 S. Plimpton, *J. Comput. Phys.*, 1995, **117**, 1–19.

52 B. R. Brooks, R. E. Bruccoleri, B. D. Olafson, D. J. States, S. Swaminathan and M. Karplus, *J. Comput. Chem.*, 2004, **4**, 187–217.

53 Y. Hou, J. X, Z. He, H. Wu and Y. Zhu, *Nano Res.*, 2023, **16**, 8036–8041.

54 R. Song, Y. Hou, Z. He, H. Wu and Y. Zhu, *Mech. Mater.*, 2024, **192**, 104986.

55 A. Stukowski, *Modell. Simul. Mater. Sci. Eng.*, 2010, **18**, 015012.

56 W. Humphrey, A. Dalke and K. Schulten, *J. Mol. Graphics*, 1996, **14**, 33–38.

57 Z. Z. He, Y. B. Zhu, J. Xia and H. A. Wu, *J. Mech. Phys. Solids*, 2019, **133**, 103706.

58 S. Le Roux and V. Petkov, *J. Appl. Crystallogr.*, 2010, **43**, 181–185.

59 T. Ozyhar, S. Hering and P. Niemz, *J. Mater. Sci.*, 2012, **47**, 6141–6150.

60 A. A. Baker, J. Sugiyama and M. J. Miles, *Biophys. J.*, 2000, **79**, 1139–1145.

61 L. M. J. Kroon-Batenburg and J. Kroon, *Biopolymers*, 2004, **29**, 1243–1248.

62 J. Sugiyama, *Macromolecules*, 1991, **21**, 4168–4175.

63 L. Fang and J. M. Catchmark, *Cellulose*, 2014, **21**, 3951–3963.

64 T. Rosen, H. He, R. Wang, C. Zhan, S. Chodankar, A. Fall, C. Aulin, P. T. Larsson, T. Lindstrom and B. S. Hsiao, *ACS Nano*, 2020, **14**, 16743–16754.

65 K. Abe and H. Yamamoto, *J. Wood Sci.*, 2005, **51**, 334–338.

66 J. H. Li, X. H. Sun, Z. Z. He, Y. Z. Hou, H. A. Wu and Y. B. Zhu, *J. Mech. Phys. Solids*, 2025, 105999.

67 K. Kulasinski, Physical and mechanical aspects of moisture adsorption in wood biopolymers investigated with atomistic simulations dissertation, ETH Zurich; 2015, DOI: **10.3929/ethz-a-010564673**.

68 M. Leonardon, C. M. Altaner, L. Vihermaa and M. C. Jarvis, *Eur. J. Wood Wood Prod.*, 2009, **68**, 87–94.